

Nanomechanical Systems for Reservoir Computing Applications

Enise Kartal, Yunus Selcuk, Humayun Ahmed, Batuhan E. Kaynak, M. Taha Yildiz, Ramazan Tufan Erdogan, Cenk Yanik, and Mehmet Selim Hanay*

Reservoir computing (RC) provides a route to use physical systems for computation and machine learning. Owing to their inherent nonlinearity, nanomechanical systems constitute an interesting technology to serve as reservoir. While RC platforms are built using microelectromechanical systems, the energy efficiency, response time, and footprint of these systems can be significantly improved by using nanoscale devices. Herein, the use of nanoelectromechanical systems (NEMS) is investigated, which can be used in RC, utilizing inherent nonlinearities and the fading memory effect from the transient response of NEMS. The smaller size and higher operating frequencies of NEMS enable faster processing rates compared to micromechanical systems, while their compact footprint, low power consumption, and ability to operate under ambient conditions simplify integration into practical applications. In modified national institute of standards and technology (MNIST) handwritten digit-recognition test, this system achieves 90% accuracy with a 3.3 μ s processing time per pixel. Also the effect of driving frequency and amplitude on NEMS classification accuracy is investigated using experiments and simulations and it is shown that no significant dependency in any of the parameters is observed. Herein, an estimate for energy consumption of core NEMS RC system on MNIST data is provided. These results highlight the potential for various applications that require efficient and fast information processing in resource-constrained environments.

memory, and transformers offer impressive capabilities, they often require substantial computing power for training deep neural network (DNN) architectures.^[1,2] Training becomes increasingly challenging in applications where miniaturized devices and low power consumption are essential, such as for applications in robotics and the Internet of Things.^[3] Resource-constrained edge computation devices operating within large networks necessitate efficient on-device processing and intelligent data analysis capabilities.^[4] Here, limitations in processing power, memory, and battery life restrict the complexity of algorithms that can be deployed on these miniature devices.

Reservoir computing (RC) is one of the approaches investigated to address the aforementioned challenges.^[5–7] Unlike traditional RNNs that require significant computational resources for training hidden layers, RC benefits from a high-dimensional reservoir of nonlinear elements to map input data to desired outputs.^[3] This process makes RC computationally efficient, providing a framework desirable for resource-constrained edge devices, enabling


on-device processing and intelligent data analysis^[8] all without sacrificing precious device size or power consumption.

Over the past decade, RC frameworks have diversified significantly. Pioneering work relied on software implementations in conventional digital systems to define a nonlinear reservoir, such as echo-state networks^[5] and liquid-state machines.^[6] More recent

1. Introduction

The development of increasingly complex architectures and data-processing tasks has pushed the boundaries of traditional computational models. While machine learning frameworks such as recurrent neural networks (RNNs), long short-term

E. Kartal, Y. Selcuk, H. Ahmed, B. E. Kaynak, M. T. Yildiz, R. T. Erdogan, M. S. Hanay
Department of Mechanical Engineering
Bilkent University
06800 Ankara, Turkey
E-mail: selimhanay@bilkent.edu.tr

 The ORCID identification number(s) for the author(s) of this article can be found under <https://doi.org/10.1002/aisy.202400971>.

© 2025 The Author(s). Advanced Intelligent Systems published by Wiley-VCH GmbH. This is an open access article under the terms of the Creative Commons Attribution License, which permits use, distribution and reproduction in any medium, provided the original work is properly cited.

DOI: 10.1002/aisy.202400971

E. Kartal, B. E. Kaynak, R. T. Erdogan, M. S. Hanay
UNAM — Institute of Materials Science and Nanotechnology
Bilkent University
06800 Ankara, Turkey

C. Yanik
SUNUM
Sabancı University Nanotechnology Research and Application Center
34956 Istanbul, Turkey

advancements have focused on enhancing the performance of RC architecture and exploring unconventional physical and materials systems to serve as a rich reservoir.^[9–11] A promising research direction explores the potential of nonlinear physical systems as computational reservoirs.^[12–14] In the mechanical domain, nonlinear microelectromechanical systems (MEMS) resonators with delay-coupled feedback were used to create virtual nodes in time and achieve RC in parity check and spoken word-recognition tasks. Recently, the transient and nonlinear responses of MEMS resonators were used for implementing RC without the need for a delay unit^[15] and the ensuing device was applied to a variety of different classification tasks. These explorations pave the way for a unique synergy between RC and miniaturized mechanical systems (MEMS and nanoelectromechanical system [NEMS]), potentially leading to compact, low-power intelligent sensors with embedded reservoir functionalities.

The use of NEMS as the computational reservoir within RC presents a significant opportunity for developing miniaturized intelligent sensors. Unlike their larger MEMS counterparts, NEMS operates at the nanoscale, offering the potential for significantly reduced power consumption due to their inherent miniaturized nature. The mechanical resonances and easily accessible nonlinear regimes^[16–20] in NEMS offer unique computational advantages as a reservoir, potentially leading to susceptible and efficient sensors capable of performing real-time data processing and analysis directly on the device.

This work investigates the application of a single nonlinear NEMS device as a computational reservoir within an RC framework (Figure 1). The input data is serialized and directly fed into the NEMS reservoir, leveraging its nonlinearity. In addition to nonlinearity, NEMS resonators provide the necessary fading

memory effect owing to their transient response: information fed into the NEMS device at different times will have compounding effects due to the finite ringdown time of the resonator. These properties, in principle, facilitate the mapping of the input signal into a high-dimensional space where distinct classes become linearly separable. The input signal sampling time is maintained below or close to the ringdown time of the system to exploit the transient dynamics of the NEMS.^[15] This configuration ensures that the reservoir response reflects a combined influence of past and current input values. The experiments were conducted under atmospheric pressure and required only standard electronics, features that enable a straightforward integration process for practical applications. Furthermore, using NEMS devices with high resonance frequencies facilitates operation on a significantly faster timescale than state-of-the-art mechanical devices, leading to a demonstrably quicker system response. We further calculate the amount of energy needed to process the MNIST data and compare it with current approaches.

2. Results/Discussion

2.1. Fabrication and Measurement of the Nanomechanical Resonator

To implement a nonlinear RC system, we utilized two devices, both based on silicon nitride. The first device is a doubly clamped silicon nitride beam (length = 10 μm , width = 400 nm, thickness = 100 nm) with a central platform (length = 2 μm , width = 3 μm , thickness = 100 nm) resonator as the core computational element (Figure 2a). Device 1 was used in studies in atmospheric conditions, whereas

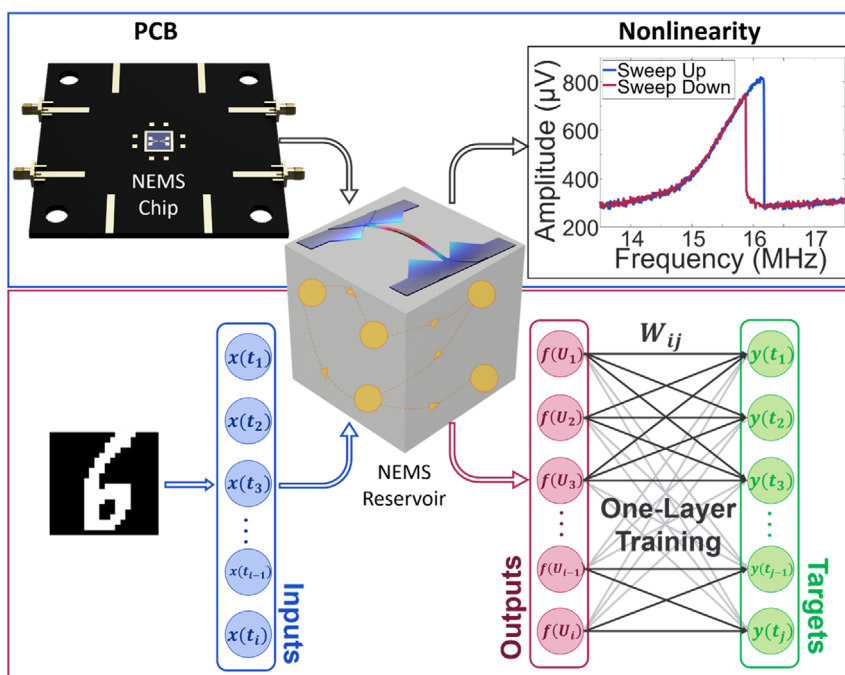


Figure 1. Reservoir computing architecture. Schematic of the nonlinear nanomechanical resonator-based reservoir computing system. The targets are the linear weighted sums of the output nodes of the reservoir. The nodes in the reservoir are the neural nodes created by the transient response of NEMS, which are connected temporally.

a slightly different device, device 2, was used in studies at high vacuum (Table 1). The fabrication of the devices was detailed in an earlier publication.^[21] Briefly, the device was fabricated on a thin silicon nitride layer deposited on a silicon substrate by low-pressure chemical vapor deposition (University Wafer). The U-shaped metal electrodes on the bridge are used for electronic transduction of the device: these features have an 80 nm width with an 80 nm gap. The fabrication^[21] starts with a two-step electron beam lithography process: the first step defines the gold electrode pattern following gold deposition and liftoff, and the second step defines the copper etch mask pattern. Subsequently, copper is deposited and lifted off to serve as a dry etch mask for the nitride beam release. Then, an anisotropic inductively coupled plasma (ICP) etch is performed to etch the silicon nitride, and finally, an isotropic silicon etch is performed using ICP to achieve beam suspension. The copper mask is removed using a wet etchant, completing the device fabrication. The chip is then placed on a printed circuit board (PCB) and wire-bonded for electronic transduction (Figure 2b).

The mechanical motion in the NEMS resonator is excited by thermoelastic actuation (Figure 2c). Here, an AC voltage is applied to the metal electrode at one side of the NEMS. The difference in thermal expansion coefficients of the silicon nitride beam and the gold electrode causes this AC voltage to induce

Table 1. NEMS properties.

Property	Device 1	Device 2
Wafer	500 μm silicon (Si)	500 μm silicon (Si)
Fabrication layer	100 nm low pressure chemical vapor deposition (LPCVD) silicon nitride (Si_3N_4)	100 nm LPCVD silicon nitride (Si_3N_4)
Shape	Paddle (beam + central platform)	Double-clamped beam
Length	10 μm	8 μm
Width	400 nm	500 nm
Thickness	100 nm	100 nm
Platform dimensions	2 μm by 3 μm	N/A
Resonance frequency	7.9 MHz	17.7 MHz
Operation pressure	1 atm	$<10^{-6}$ Torr
Quality factor (Q)	≈ 100	≈ 5540
Young's modulus	≈ 250 GPa	≈ 250 GPa
Density	≈ 3100 kgm^{-3}	≈ 3100 kgm^{-3}
Bandwidth	7.9×10^4 Hz	3.2×10^3 Hz
Actuation mechanism	Thermoelastic	Thermoelastic
Sensing mechanism	Piezoresistive	Piezoresistive
Operation temperature	300 K	300 K

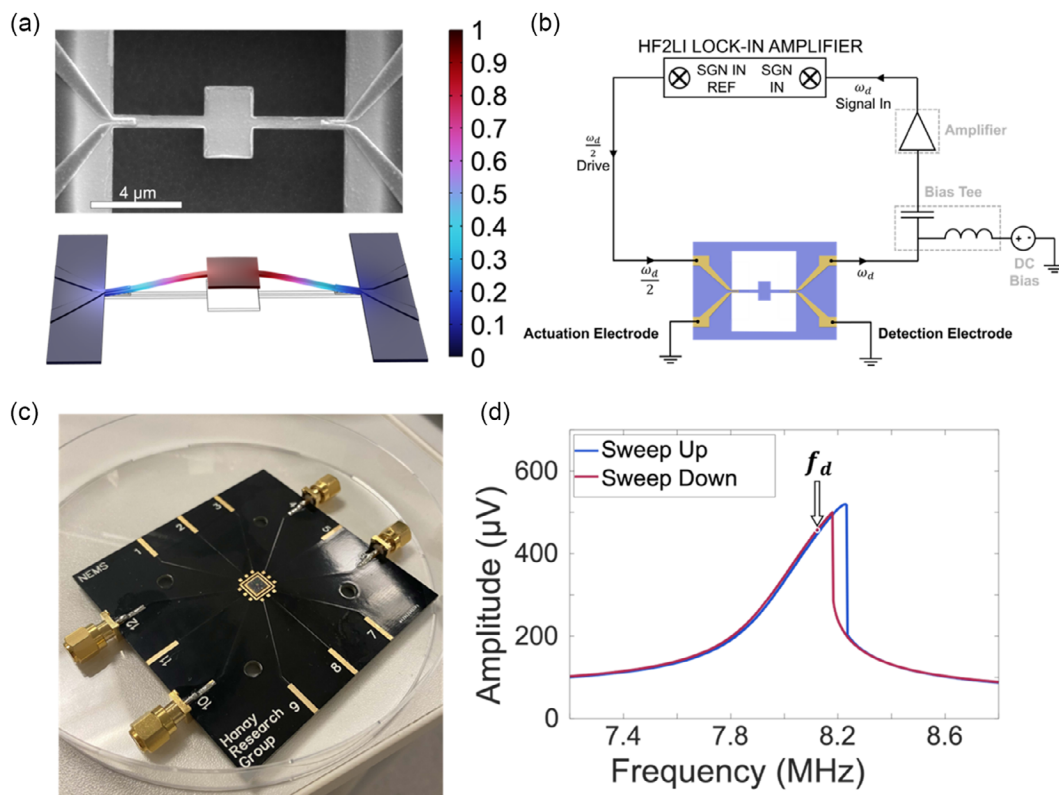


Figure 2. Nanoelectromechanical resonator and the first mode open-loop sweep. a) The scanning electron microscope (SEM) image of the device used in the experiments is shown in the top portion, and the COMSOL simulation for the fundamental mode used in the experiments. The colormap indicates the displacement amplitude. b) Measurement circuitry. c) The NEMS chip embedded in a PCB for electronic measurements. d) Open-loop frequency sweep of the resonator at its first mode under atmospheric conditions. The frequency indicated by the arrow is the nonlinear driving frequency of the resonator, 8.12 MHz.

varying degrees of thermal expansion in both the electrodes and the beam, leading to a thermally induced stress profile. The periodic heating and cooling due to the AC-voltage-induced mechanical stress are proportional to the square of the input voltage; thus, the electronic drive frequency is adjusted to match half the mechanical resonance frequency. Earlier studies^[22] indicated that the efficiency of thermal actuation decreases at high frequencies, due to the thermal time constant of the material, which is estimated to correspond to 40 MHz for silicon nitride. Since the resonance frequencies of the devices used in this work are below this limit, we do not expect a significant degradation in actuation performance due to thermal time constant.

To read out the NEMS motion, we use the electrode on the other side of the device. As this electrode undergoes periodic strain, its resistance changes due to geometry-induced piezoresistivity^[22,23] since the readout electrode is gold, and piezo effects due to band bending are negligible. As NEMS undergoes motion, the gold electrode elongates and shrinks in response. The changes in electrode length modify the resistance of the electrode accordingly (as $R = \rho LA^{-1}$ where ρ is the resistivity of the metal, L is the beam length, A is the beam cross-sectional area). In addition to the change of axial dimensions, the transverse dimensions of the electrode also change via the Poisson ratio, further strengthening the change in metallic resistance.

We bias this resistor with a DC source by using a bias-T component. The DC bias combines with the dynamical part of the resistance to generate an AC signal at the NEMS frequency. The AC signal at the output can pass through the capacitive component of the bias-T and reach the amplification stage. This signal is measured by first using a low-noise amplifier, followed by a lock-in amplifier (LIA) (Zurich Instruments HF2LI). Frequency sweep of the NEMS device in the nonlinear region is shown in Figure 2d: the hysteresis due to Duffing nonlinearity is evident when the upward and downward frequency sweeps are compared. Later on, the drive portion of the NEMS device is modulated to encode the digit information for the MNIST classification task: this is explained in more detail later.

2.2. RC System Based on a Nonlinear Nanomechanical Resonator

The NEMS resonator exhibits characteristics of a typical underdamped second-order oscillator system. Its inherent utility stems from a combination of the Duffing nonlinearity and the transient exponential nonlinear response arising from its second-order dynamics. This combination guarantees rich nonlinear dynamics within the single resonator reservoir, enabling efficient processing of pattern-recognition tasks.

Thermoelastic actuation provides the driving mechanism for the resonator, and the readout mechanism is piezoresistive detection.

The natural frequency and quality factor (Q) of the NEMS significantly influence the performance of the RC system. A sufficient quality factor is preferred to ensure adequate memory capacity, as it directly influences the ringdown time ($T = 2Qf_n^{-1}$) of the resonator. Characterization of the nonlinear dynamic response of the beam is critical as it is the primary source of nonlinearity within the reservoir. Multiple frequency sweeps are

conducted to identify suitable driving frequencies (f_d) and excitation amplitudes that produce the desired nonlinear state for achieving rich reservoir dynamics.

Figure 2d illustrates the nonlinear frequency response of the NEMS resonator. To guarantee a high signal-to-noise ratio and stable amplitude output, the NEMS was driven at a frequency (f_d point) slightly lower than the frequency value corresponding to the front bifurcation point of the hysteresis loop, as shown in Figure 2d. Another reason for choosing a value lower than the front bifurcation point was to prevent switching between two stable branches during the experiments,^[19] since the predominant frequency drift in the experiments was toward lower values.^[24,25]

Traditional time-delayed RC requires careful optimization of various parameters to generate a reservoir state with rich representational power, which ultimately determines the effectiveness of the system. In RC implementation, an input mask function serves as a critical element, which serializes the input signal and maximizes accessible dimensionality. In prior works, it was discussed that a self-masking procedure occurs within the reservoir. The masking procedure modulates the signal with arbitrarily fixed weights and feeds the response of the reservoir back to the system, thus creating an artificial fading memory. However, this process comes with various hyperparameters, and designing an optimal mask function can be challenging. Instead, the experimental setup of this work adopts a similar core concept developed in ref. [15] where the masking procedure was removed. This simplification leads to exploring and focusing more on the intrinsic nonlinearities and fading memory of the MEMS in performing RCs. We used this architecture in the smaller NEMS devices to benefit from their higher resonance frequencies and increase the processing speed.

The architecture consists of three main parts: an input layer, a reservoir, and an output layer. The input signals are preprocessed and vectorized before being fed into the reservoir to ensure compatibility with the NEMS reservoir, which operates on vectorized data. Subsequently, the normalized vector is fed as the modulation signal, where the carrier signal drives the NEMS resonator to the nonlinear region of its fundamental mode. This modulation serves to push the NEMS into the nonlinear operational regime, a key factor for exploiting its information-processing capabilities within the RC framework. Within the reservoir, the processing occurs, incorporating the input signal and the nonlinear system response. Finally, the reservoir states are sampled and used for training and testing procedures through a linear regression algorithm.

A crucial parameter in this process is the separation time, which dictates the frequency of updates on the input signal. In other words, the separation timescale denotes the duration of each information unit (e.g., pixel value) presented to NEMS by modulating the drive signal near resonance. The selection of separation time is critical: choosing a separation time too close to the ringdown time diminishes the memory capacity of the output signal. Conversely, a minimal separation time ($<0.1T$) hinders the ability of the reservoir to effectively map the input data into a higher-dimensional space, an essential step for subsequent classification tasks.

The proposed single-resonator RC experimental setup offers several advantages contributing to its practicality and efficiency. First, the system operates entirely under atmospheric conditions,

eliminating the need for complex vacuum systems. The operation in ambient pressure reduces the quality factor: as a result, the ringdown time decreases, enabling a fast system response. Importantly, NEMS resonator can still generate a nonlinear response even when it possesses a low quality factor (≈ 50) in ambient conditions.^[26] Operating at atmospheric conditions and with low power consumption provides an advantage for the potential of NEMS-based RC systems in customer electronics, edge computation, and the internet of things.

Beyond its operational simplicity, the system benefits from the dynamical properties of the NEMS resonator. Due to its microsecond-scale ringdown time, training large datasets, can be completed within minutes including data preprocessing. Additionally, the compact device footprint facilitates seamless integration into diverse dimensional systems, highlighting its potential for broad applicability.

2.3. Introducing MNIST Data

The experimental setup, depicted in **Figure 3**, utilizes an arbitrary waveform generator (AWG) to create a modulated driving signal for the NEMS. This modulated signal incorporates the vectorized input data, containing pixel brightness information for each image in the dataset, and a basic sinusoidal wave with an amplitude and frequency chosen to set the NEMS in the nonlinear driving regime. Essentially, the AWG performs amplitude modulation on the input data, where the modulation amount is proportional to the brightness of the pixel being processed:

$$V_{\text{signal}} = \frac{(1 + m(t))}{2} V_d \cos(\omega_d t/2) \quad (1)$$

where V_d is the initial nonlinear driving amplitude and $m(t)$ contains the brightness information of each pixel, normalized to be between 0 and 1, and the duration of each pixel information that is supplied to the NEMS device. The electronic signal driving the NEMS resonator is provided at half of the mechanical driving frequency ($\omega_d/2$), since the thermoelastic actuation used here produces mechanical strain at twice the excitation

frequency.^[22,23,27] Similarly, the modulation term $m(t)$ undergoes the square transformation by the electronic to mechanical transduction: we consider this drive-related nonlinearity (in addition to mechanical Duffing nonlinearity) as part of the total nonlinear response of the architecture.

The electronic signal, modulated by the pixel brightness data, drives the NEMS resonator mechanically. The NEMS displacement is read out at the other end of the structure by the piezoresistive detection. The system employs an LIA for readout purposes. The LIA demodulates the output signal from the NEMS resonator using an external reference input signal, a pure sinusoidal provided by the second (and phase-synchronized) output channel of the AWG at ω_d : this reference input mirrors the second harmonic of the sinusoidal carrier (at $\omega_d/2$). The demodulated output signal, containing the processed information, is then collected and utilized for the training process.

This simple single-resonator RC experimental setup offers several advantages. It reduces overall complexity compared to most other RC systems while maintaining flexibility and improving information-processing efficiency. The AWG's ability to seamlessly integrate the input data with the driving signal through amplitude modulation is another core benefit. Furthermore, the demodulation process facilitated by the LIA ensures the extraction of relevant information from the NEMS output, contributing to a streamlined and efficient information-processing pipeline within the RC system.

2.4. MNIST Handwritten Digit–Recognition Task

After obtaining the basic parameters of the NEMS resonator with the experimental system mentioned earlier, the classification performance of the system was evaluated using the MNIST handwritten digit dataset. MNIST, a widely recognized benchmark dataset for handwritten digit classification, comprises 28×28 pixel images offering a well-defined task for evaluating the nonlinear mapping properties of the NEMS reservoir (Figure 3).

The MNIST dataset images were cropped from their original size of 28×28 pixels to a smaller dimension of $22 \times 20 = 440$

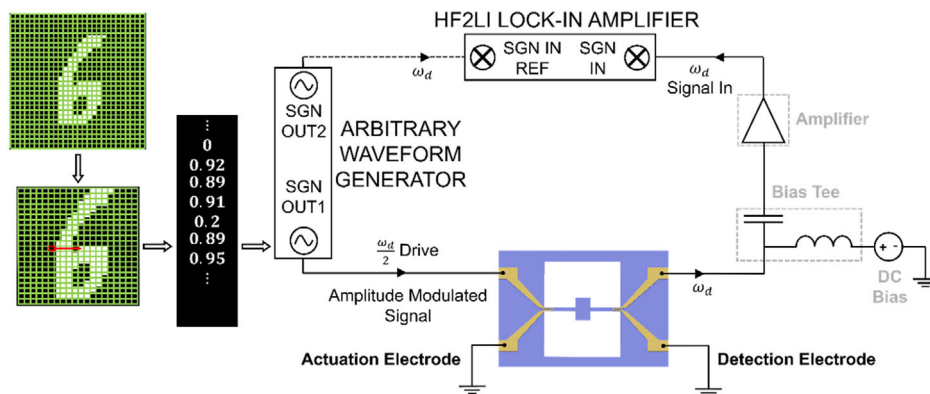


Figure 3. Schematic of the experimental setup and reservoir computing system. Cropped images with high information content are uploaded to the AWG as vectors containing the grayscale values corresponding to the brightness of each pixel (normalized to unity for a fully white pixel). In the bottom middle of the circuit schematic, a render of the resonator can be seen. An AC signal (sinusoidal wave) modulated with the input vectors is fed to the actuation electrode of the resonator, and the reading is performed via the detection electrodes using a lock-in amplifier, which also receives an external reference signal (unmodified sinusoidal wave) from a phase synchronized second channel of the same AWG instrument.

pixels as a preprocessing step, removing potentially irrelevant blank peripheral regions. Preprocessing reduces redundant information within the input signals before feeding them into the reservoir (Figure 3) by cropping the images to their more informative parts. Subsequently, these cropped images are vectorized, resulting in a representation where each image is transformed into a 440-element vector. The form of supplied vector values of individual pixels and the response of the nonlinear NEMS resonator are shown in **Figure 4**.

The vectorization of the images facilitates compatibility with the experimental setup with the NEMS resonator. As the serialized data (440 levels for each image) is fed into NEMS at the input port (Figure 4a), the NEMS output was collected in corresponding packages of 440 levels, forming the reservoir output features (Figure 4b). These 440 features are then connected to 10 output perceptrons, with an identity activation function. The output layer is passed through a Softmax layer to obtain the probability distribution of the predicted class of the input. Softmax provides good accuracy for problems with multiple classes and single labels, such as the digit-recognition task. The training is done by optimizing the log-loss function with an L2 regularization term to be small, i.e., until the loss function no longer changes by an arbitrarily set tolerance value (10^{-4}) for 10 consecutive iterations. The loss function is expressed as

$$L(p, q) = - \frac{\left(\sum_{j=0}^{n_{\text{samples}}} \sum_{i=0}^{n_{\text{classes}}} p(x_{ij}) \log(q(x_{ij})) \right) + \text{L2Regularization}}{\text{SampleSize}} \quad (2)$$

where p is the true probability distribution, q is the predicted probability distribution, and the L2 regularization term is expressed as

$$\text{L2Regularization} = \left(\alpha \sum_{n=0}^{n_{\text{features}}} \sum_{i=0}^{n_{\text{samples}}} w_{ni}^2 \right) \quad (3)$$

where α is the regularization strength constant and w is the weight between the NEMS output features and the output layers. The Softmax function is defined as follows:

$$\text{Softmax}(z_i) = \frac{\exp(z_i)}{\sum_{j=0}^n \exp(z_j)} \quad (4)$$

The weight optimization with respect to the loss function is achieved by the backpropagation algorithm with a learning rate of 0.001. To increase the efficiency, the adaptive moment estimation (Adam) solver was used. In total, we have utilized 24000 images from the MNIST dataset (due to the memory capacity of an electronic instrument in the setup, not all 60000 we used). From these 24000 images, 2400 of which were randomly selected as test data. K-fold cross validation is applied for tenfold, and the average accuracy from the validation test can be seen in **Table 2**. The confusion matrix for a set of parameters (separation time = 3.3 μs) is shown in **Figure 5**.

A crucial factor influencing the reservoir dynamics of the NEMS is the separation time.^[28] The separation time between two pixels can be defined with the parameter $\theta = nT$ ($n > 0$) where T stands for the ringdown time of the NEMS resonator. The experiment was conducted at different separation times; however, no significant trend was observed for the range of parameters tested in this study. In this work, the lock-in time constant was kept constant at 0.77 μs for all different test conditions; this way, the noise was filtered in the same manner across different separation times.

Table 2. Accuracy for the MNIST digit-recognition test for different separation times.

$n = \frac{\text{SeparationTime}(\theta)}{\text{RingdownTime}(T)}$	Separation time, θ [μs]	Average training accuracy [%]	Average validation accuracy [%]	Test accuracy [%]
0.25	3.3	93.3	90.3	90.7
0.5	6.6	93.6	89.4	89.0
1	13.2	92.7	88.2	88.1
2	26.4	94.7	90.4	90.0
4	52.8	94.8	90.5	90.6

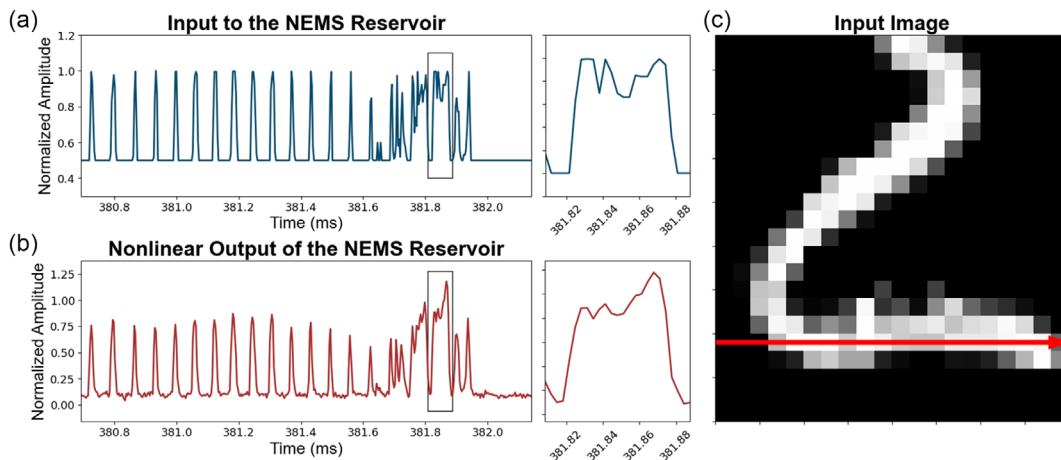


Figure 4. Comparison of signals supplied to and read out from the NEMS resonator. a) One of the images was provided to the NEMS reservoir as input. As the brightness of the pixel increases, so does the corresponding input drive level (y axis). b) The output signal after processed by the nonlinear NEMS resonator. c) The specific image being processed by the NEMS. Red arrow indicates the row being processed as highlighted in the insets.

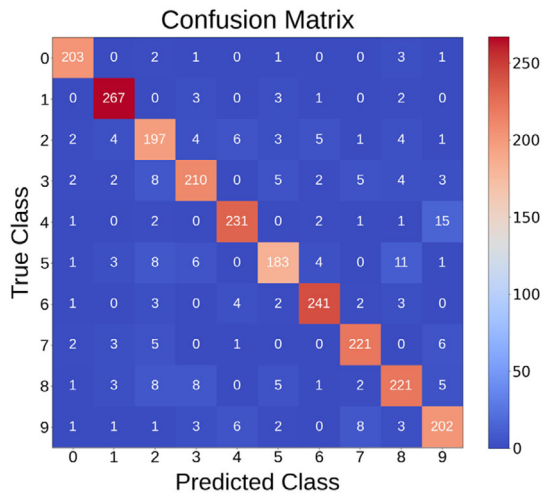


Figure 5. Confusion matrix of the system for separation time = 3.3 μ s, i.e., $n = 0.25$. Due to the random selection of test data, there are small asymmetries between the occurrence of different classes.

The ringdown time of the NEMS resonator (13.2 μ s) sets the duration for which each image is processed. In this case, for the fastest processing of the data, each image is processed by NEMS within 3.3 μ s and at 90% accuracy. A notable difference lies in the ringdown times observed in our study compared to existing literature.^[15] A recent work of RC with no delayed feedback loop^[10] reports significantly higher ringdown times, ranging from 16 to 35 ms. Other works with low ringdown times close to the values reported in this work, such as the one presented in ref. [29], depend on delayed feedback loops.

2.5. Experiments under Vacuum—High-Quality-Factor NEMS

To explore the effect of quality factor on the performance, we have also conducted experiments under high vacuum conditions ($<10^{-6}$ Torr) with an NEMS doubly clamped beam with dimensions of 8 μ m length, 500 nm width, and 100 nm thickness, with

a resonance frequency of 17.7 MHz. Experiments with four different driving frequencies at two different separation times were conducted (**Figure 6**). Owing to operation under vacuum, the quality factor of the device was close to 5500 with a ringdown time of 620 μ s. In this case, the system was operated on the high-amplitude (forward sweep) branch of the nonlinear response (Figure 6). With this system, we have investigated the effect of biasing point along the high-amplitude branch by changing the drive frequency. The experiment was conducted on all 70000 images of the MNIST digit dataset, 10000 of which are test images. As can be seen from Figure 6a, the obtained accuracy has only a weak dependence on the operation frequency, peaking near the center. For Figure 6a, the separation time between the digits was 40 μ s ($\theta = 0.07$), when the separation time is doubled to 80 μ s ($\theta = 0.13$), NEMS has more time to respond to each pixel, and the accuracy values have increased slightly (Figure 6b). For this larger separation time, the accuracy again only weakly depended on the frequency of operation, varying by only several percent around 90%.

To understand the NEMS as a reservoir, it is instructive to look at the nonlinear input–output relationship imposed by NEMS (**Figure 7a**). For driving at weak nonlinearity, such as at 17.72 MHz (dark green trace), NEMS acts as a saturating amplifier: for low drive powers (dark pixels), NEMS produce a linear output; but for high drive powers (bright pixels), the outputs is also constant. At higher drive values, the shift between the low-amplitude and high-amplitude pixels happens more sharply (e.g., the blue trace at 17.75 MHz). This nonlinear relationship has a similar shape at different operation points; as such, the performance does not vary significantly along the spectrum.

2.6. Simulating Nonlinear NEMS Dynamics

To obtain insight into the performance and characteristics of NEMS as a reservoir, we have conducted simulations to capture the nonlinear and transient dynamics of NEMS resonators with Duffing nonlinearity. The equation of motion for the system reads

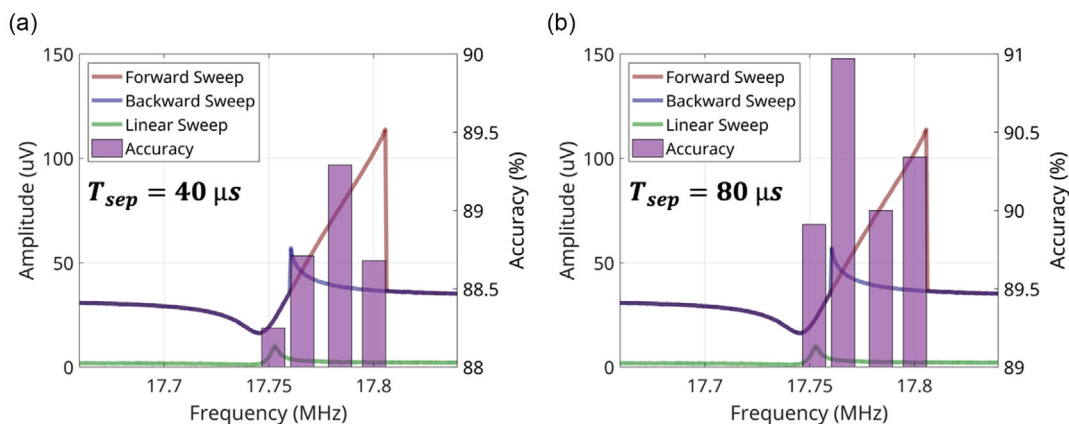


Figure 6. The classification performance of the NEMS resonator in vacuum for two different separation times: a) 40 μ s and b) 80 μ s. The NEMS is operated at different frequencies on the forward-sweep branch in the linear regime. The backward sweep and linear sweeps are provided to form reference points; they were not utilized as operating points.

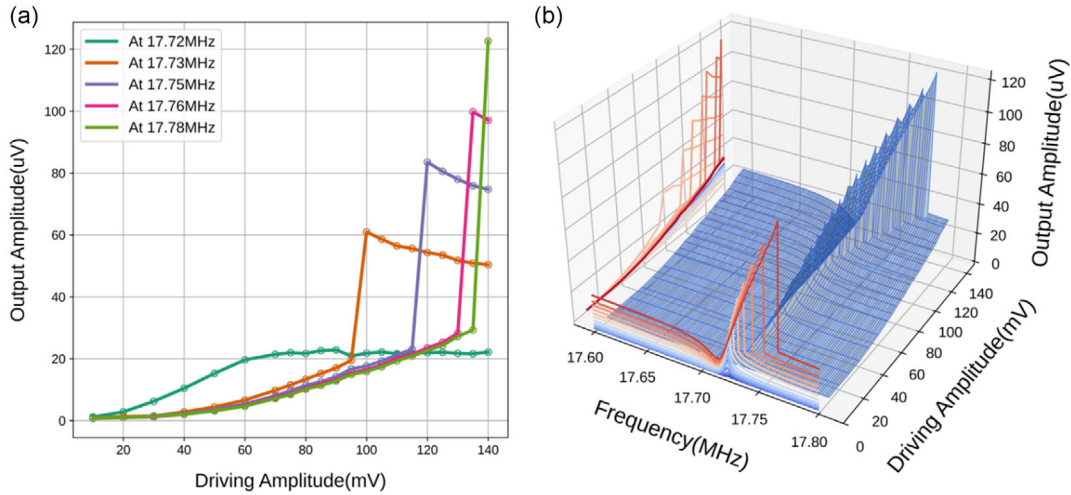


Figure 7. a) The input–output relationships imposed by nonlinear NEMS at different frequencies (i.e., different operation points). The pixel values change the driving amplitude (x axis), and the NEMS generates a nonlinear response (y axis) as seen in the output amplitude. b) NEMS as a nonlinear component, the input–output relationships as a function of driving amplitude and frequency.

$$\ddot{X} + \frac{\omega_n \dot{X}}{Q} + \omega_n^2 X + \alpha X^3 = F_d(t) \quad (5)$$

where x , \dot{x} , and \ddot{x} represent the displacement, velocity, and acceleration of the resonator, respectively. ω_n is the natural angular frequency in the linear regime, Q is the quality factor, and $F_d(t)$ is the time-dependent driving force per unit mass. Notably, α is the Duffing coefficient indicating the degree of nonlinearity in the restoring force.^[16] For the numerical study, we have investigated the performance of an NEMS resonator in atmospheric and vacuum conditions. The main difference between the two conditions stems from the Q . By using experimentally observed values for the devices used in this work, we set $Q_{\text{air}} = 100$ for operation in air, and $Q_{\text{vacuum}} = 5500$ for operation in vacuum. To convert Equation (5) into a form suitable for numerical simulations, and injection of the information content (e.g., pixel brightness values of an image), we rewrite the equation in nondimensionalized form as detailed in ref. [16]:

$$\ddot{X} + \varepsilon \dot{X} + X + X^3 = g \varepsilon^{\frac{1}{2}} \frac{(1 + m(\tau))}{2} \cos(\Omega_d \tau) \quad (6)$$

Here, $\varepsilon = Q^{-1}$, the amplitude X is scaled by the $\sqrt{\alpha}$, τ is scaled by ω_n , g is the dimensionless forcing term, $m(t)$ contains the information content in a time-series form, and Ω_d is the normalized driving frequency. The solution of Equation (6) is obtained numerically via the classical fourth-order Runge–Kutta method, and the details are given in Section S1, Supporting Information. For each given image in the MNIST training dataset, the corresponding signal $m(t)$ is provided, and Equation (6) is solved to obtain the scaled amplitude $X(t)$ which is then used to compute the root-mean-squared displacement of the NEMS, which is the actual parameter measured in the experiments.

$$X_{\text{rms}} = \sqrt{\frac{1}{t_s} \int_{p \times t_s}^{(p+1) \times t_s} X^2 dt} \quad (7)$$

where p is the pixel number in the 1D pixel array and t_s is the separation time between two pixels. The X_{rms} value represents the NEMS output after a pixel is processed, and an array of X_{rms} values are then used to train the final layer, mimicking the process flow carried out in the experimental section.

To recapitulate the experimental conditions accurately, the value of g must be adjusted to match the driving force in the experiments. We obtain the value of g by first calculating the normalized frequency shift in the maximum point of the resonance curve as the response becomes nonlinear. By finding the value of g in simulations that corresponds to the same amount of frequency shift in the experiments, we run the simulations. As an example, for the experiments in Figure 3, the normalized shift in the maximum point of the resonance curve with respect to the linear curve was 1.4%, and the corresponding drive level for the simulations was $g = 2.4$.

After matching the simulation conditions to the experiments, we conducted the simulations for the nonlinear and transient dynamics of NEMS and fed the resulting waveforms to the same final layer used in the experiments. We first investigated the effect of driving frequency (Figure 8a). Here, the accuracy reaches a 92% level at the two sides of the resonance curve; however, there is a drop in accuracy when operated within the range of bistability (e.g., between points B and Q in Figure 8a). A similar drop was observed in experiments, which was attained to an occasional drop of the nonlinear system to the lower amplitude branch of the resonance when operated in the bistability window. Such occasional transitions to the lower branch are expected to limit the classification accuracy since the signal-to-noise ratio from the NEMS is degraded. Both the experiments and simulations indicate that, within the existing scheme, it is better to avoid the bistability window (e.g., point Q).

2.7. Energy Consumption

A growing concern in the field of ML is energy consumption: in this regard, it is beneficial to provide a preliminary estimate for

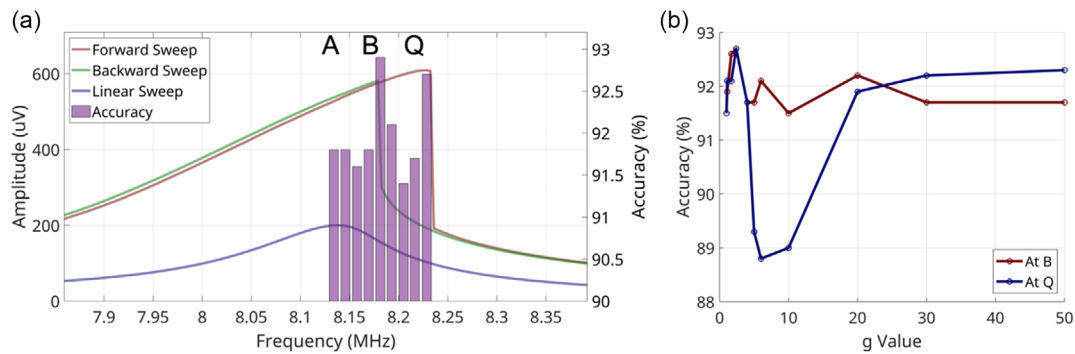


Figure 8. Simulation results for classification performance. a) Performance as a function of driving frequency on the forward sweep. Points A and Q show the location of the (linear) resonance frequency and the edge of the branch jump for the forward sweep. Point B is located just before the midway point, as in Figure 2d. The accuracy changes only within a few percent as a function of driving frequency, in agreement with the experiments. b) The effect of increasing drive strength, such that $g = 1$ at the onset of nonlinearity. For point B, which is outside the bifurcation window, the trend is constant within 2%. The point Q, which can access the lower branch, follows a more varied trend.

the energy consumption of the core NEMS RC unit and compare it to the benchmark values. For benchmarking, a recent paper studied the energy consumption of training an MNIST data set^[2] and reports 11.3 Wh for a Gemini GPU and 1.6 Wh for a central processing unit (CPU)-based system (only the computational core components, such as processor and RAM were considered; and the system was trained for 5 epochs). In our work, the NEMS resonator was driven by a 700 mV AC signal at the drive port, and 400 mV bias on the readout port: with $R_{\text{NEMS}} = 50 \Omega$ on both sides, we get a power consumption of 13 mW on the NEMS. The power consumption of the first-stage amplifier used was ≈ 450 mW (15 V, 30 mA current). Thus, the core part of the system providing NEMS with drive and readout amounts to 463 mW. Other critical components of the system are presented in the power consumption budget (Table 3), which indicates that the essential power consumption of the system is close to 620 mW.

For the 24000 images of MNIST, the total duration of training was ≈ 2 min: for the full 60000 images, the duration can be extrapolated to 4.5 min; and the power consumption becomes 45 mWh, which is an order-of-magnitude smaller than a single epoch of the CPU-based system (320 mWh per epoch) and two orders of magnitude smaller than the GPU-based system (2.2 Wh per epoch). The energy calculation for the NEMS RC system did not include the energy cost of training the single-layer network in the CPU to

Table 3. Energy budget for the core components of the NEMS RC system.

Subsystem	Model	Power
NEMS drive electrode	700 mV _{rms} AC signal driving 50 Ω , with a source impedance of 50 Ω	20 mW
NEMS readout electrode	400 mV DC signal biasing 50 Ω	3 mW
First-stage amplifier	15 V, 30 mA	450 mW
Phase-sensitive detection	Mixers and low-pass filtering. Two 1 V carrier signals, generated by 50 Ω sources	40 mW
Analog-to-Digital Conversion (ADC)	Typical component-level value is taken for a 100 MHz sampling time, 12-bit resolution	100 mW
Total	–	620 mW

since single-layer training is clearly much less power intensive than training a network with deep layers. The low power consumption arises due to the nanoscale size of the NEMS device, small voltage levels needed to drive the NEMS to its nonlinear regime, and the absence of any high-power auxiliary components such as vacuum systems, cryogenics, and lasers.

We note that the NEMS system provides energy efficiency mostly in the training phase. For the inference phase, a DNN needs to make only a single forward pass, which results in an energy consumption a few orders of magnitude smaller (depending on the number of epochs, batch size differences in inference vs training) compared to training. For optoelectronic RC systems, we estimate an amount of energy consumption similar to NEMS levels for training (Section S2, Supporting Information).

The serial nature of data injection and processing in NEMS can increase the processing times significantly for data series with larger information content (e.g., HD images). It is envisaged that a network of interacting NEMS devices can be used to provide the necessary parallelism for such applications. Furthermore, one advantage of using physical systems, especially exquisite sensors such as NEMS, it is possible to accept physical signals directly from the environment. The direct transduction of sensory signal can take the form of acoustic,^[30] vibrational,^[31] photonic,^[32] or spectroscopic^[33] information.

We finally note that the obtained accuracy level (close to 90%) is slightly below what can be obtained by linear neural networks implemented in a digital system (92%). This observation questions why NEMS nonlinearity provided further utility in classification performance. While it is possible that the physical noise present in the experiments limits accuracy, the numerical simulations indicate that even in the absence of noise, NEMS can reach only 92%. We thus conclude that when NEMS nonlinear response is used as described here (as a nonlinear amplifier with saturation), it is not suitable in tasks such as MNIST, possibly due to the limited expressibility of the nonlinear operation conducted by the NEMS. The field is open to investigate whether different utilization of NEMS nonlinearity can be more conducive, and whether different types of problems (such as time-series data) are more suitable to be processed by the NEMS reservoir.

3. Conclusion

The experimental analysis of the resonator's response and subsequent testing on the MNIST dataset demonstrate a classification test accuracy reaching above 90% for handwritten digits, suggesting the potential of this approach for facilitating hardware implementation of RC and paving the way for future applications leveraging NEMS technology. An important parameter for RC systems is the relaxation time of the physical system.^[28] A comparison of the classification rates for different technologies and studies, based on relaxation times, is summarized in **Table 4**. We have also investigated the effects of driving power and frequency of operation on accuracy; however, no strong trends were observed.

This work presented a simplified, single-resonator RC system operating under atmospheric conditions that leverages the inherent nonlinearities of an NEMS resonator. This approach eliminates complex vacuum setups, enabling faster and more efficient experimentation compared to traditional MEMS RC systems with significantly longer ringdown times. Additionally, the NEMS resonator's ringdown decay time allows for experiments to be completed within minutes for small data sets, and its compact size facilitates low energy costs and capability for scaling up. These combined advantages highlight the practicality and broad

Table 4. A comparison of ringdown/relaxation time scales of recent reservoir computing work.

Reference	Publication [year]	Technology	Ringdown/relaxation time
[15]	2021	MEMS resonator	≈16 ms
[29]	2021	MEMS resonator	Few microseconds
[34]	2021	MEMS resonator	≈330 μs
[35]	2020	MEMS resonator	≈96 μs
[36]	2022	Photo-synaptic memristor array	29–280 ms
[37]	2022	3D memristor	≈600 μs
[38]	2022	3D dynamic memristor array	Few microseconds
[13]	2021	2D memristor	≈100 ms
[12]	2021	Dynamic memristor	≈400 μs
[39]	2020	Memristor network	≈100 ms
[40]	2019	Magnetic skyrmion memristor	≈25 ns
[41]	2022	Optoelectronic synapse on van der Waals layer	30–900 ms
[42]	2021	Biocompatible organic electrochemical network	≈100 ms
[43]	2023	Ferroelectrics	12–280 ms
[44]	2022	Ferroelectric Field-effect transistor (FET)	≈100 ns
[45]	2021	Photonics	Range of picoseconds to microseconds
[46]	2021	Spin-torque nano-oscillator	≈200 ns
[47]	2021	Spintronics	10–100 ns
[48]	2020	Spintronics	hundreds of ns
[49]	2019	Spin-torque nano-oscillator	≈4 ns
[50]	2021	Stripe magnetic garnet	Few nanoseconds

applicability of this RC architecture with nanoscale, top-down engineered devices.

[A preprint version of this work has been submitted to Arxiv. Code and data are available from the authors upon reasonable request.]

Supporting Information

Supporting Information is available from the Wiley Online Library or from the author.

Acknowledgements

The authors thank Mert Göksel and Alper Demir for useful discussions and the peer reviewers for useful suggestions. B.E.K. and M.S.H. built the hardware architecture; B.E.K. designed the devices; C.Y., E.K., B.E.K., and R.T.E. fabricated the devices; E.K., B.E.K., and Y.S. conducted the experiments; YS and EK optimized the experimental parameters and generated the plots; Y.S., M.T.Y., and E.K. conducted pre- and post-processing of the data; H.A. conducted the simulations; E.K., B.E.K., and M.S.H. wrote the manuscript.

Conflict of Interest

MSH is a cofounder in Sensonance Muhendislik, the other authors declare no competing interests.

Author Contributions

Enise Kartal: conceptualization (equal); data curation (equal); investigation (equal); methodology (equal); software (equal); visualization (equal); and writing—original draft (equal). **Yunus Selcuk:** data curation (equal); investigation (equal); methodology (equal); software (equal); visualization (equal); and writing—original draft (equal). **Humayun Ahmed:** formal analysis (equal); software (equal); and writing—review and editing (supporting). **Batuhan E. Kaynak:** conceptualization (supporting); investigation (supporting); methodology (supporting); and writing—original draft (supporting). **M. Taha yildiz:** conceptualization (supporting); investigation (supporting); methodology (supporting); and software (supporting). **Ramazan Tufan Erdogan:** investigation (supporting) and methodology (supporting). **Cenk Yanik:** methodology (supporting). **Mehmet Selim Hanay:** conceptualization (equal); project administration (lead); validation (equal); visualization (equal); and writing—original draft (equal). **Enise Kartal** and **Yunus Selcuk** contributed equally to this work.

Data Availability Statement

The data that support the findings of this study are available from the corresponding author upon reasonable request.

Keywords

energy efficiencies, microelectromechanical systems, nanomechanical systems, nanoelectromechanical systems, nonlinear systems, physical neural networks, reservoir computing

Received: November 11, 2024

Revised: March 29, 2025

Published online: May 8, 2025

- [1] S. Shankar, A. Reuther, *2022 IEEE High Performance Extreme Computing Conference (HPEC)*, IEEE, Piscataway, NJ **2022**.
- [2] L. Bouza, A. Bugeau, L. Lannelongue, *Environ. Res. Commun.* **2023**, *5*, 115014.
- [3] X. Liang, J. Tang, Y. Zhong, B. Gao, H. Qian, H. Wu, *Nat. Electron* **2024**, *1*.
- [4] D. Banerjee, T. Kotooka, S. Azhari, Y. Usami, T. Ogawa, J. K. Gimzewski, H. Tamukoh, H. Tanaka, *Adv. Intell. Syst.* **2022**, *4*, 2100145.
- [5] H. Jaeger, Bonn, Germany: German National Research Center for Information Technology GMD Technical Report **2001**, 148, 34.
- [6] W. Maass, T. Natschläger, H. Markram, *Neural Comput.* **2002**, *14*, 2531.
- [7] D. Verstraeten, B. Schrauwen, M. D'Haene, D. Stroobandt, *Neural Networks* **2007**, *20*, 391.
- [8] S. Kokalj-Filipovic, P. Toliver, W. Johnson, R. Miller, **2021 Reservoir-Based Distributed Machine Learning for Edge Operation of Emitter Identification**, MILCOM 2021, IEEE, San Diego, CA pp. 96-101.
- [9] M.-K. Song, J.-H. Kang, X. Zhang, *ACS Nano* **2023**, *17*, 11994.
- [10] G. Milano, K. Montano, C. Ricciardi, *J. Phys. D: Appl. Phys.* **2023**, *56*, 084005.
- [11] H. Tanaka, M. Akai-Kasaya, A. Termehousefi, L. Hong, L. Fu, H. Tamukoh, D. Tanaka, T. Asai, T. Ogawa, *Nat. Comm.* **2018**, *9*, 2693.
- [12] Y. Zhong, J. Tang, X. Li, B. Gao, H. Qian, H. Wu, *Nat. Comm.* **2021**, *12*, 408.
- [13] L. Sun, Z. Wang, J. Jiang, Y. Kim, B. Joo, S. Zheng, S. Lee, W. J. Yu, B.-S. Kong, H. Yang, *Sci. Adv.* **2021**, *7*, eabg1455.
- [14] Z. Qi, L. Mi, H. Qian, W. Zheng, Y. Guo, Y. Chai, *Adv. Mater.* **2023**, *33*, 2306149.
- [15] J. Sun, W. Yang, T. Zheng, X. Xiong, Y. Liu, Z. Wang, Z. Li, X. Zou, *Microsyst. Nanoeng.* **2021**, *7*, 83.
- [16] R. Lifshitz, M. C. Cross, *Rev. Nonlinear Dyn. Complexity* **2008**, *1*.
- [17] M. H. Matheny, L. G. Villanueva, R. B. Karabalin, J. E. Sader, M. L. Roukes, *Nano Lett.* **2013**, *13*, 1622.
- [18] C. Samanta, N. Arora, K. K. V., S. Raghavan, A. K. Naik, *Nanoscale* **2019**, *11*, 8394.
- [19] M. Yuksel, E. Orhan, C. Yanik, A. B. Ari, A. Demir, M. S. Hanay, *Nano Lett.* **2019**, *19*, 3583.
- [20] Z. Li, M. Xu, R. A. Norte, A. M. Aragón, P. G. Steeneken, F. Alijani, *Comm. Phys.* **2024**, *7*, 53.
- [21] B. E. Kaynak, M. Alkhaled, E. Kartal, C. Yanik, M. S. Hanay, *Nano Lett.* **2023**, *23*, 8553.
- [22] I. Bargatin, I. Kozinsky, M. L. Roukes, *Appl. Phys. Lett.* **2007**, *90*, 093116.
- [23] M. Li, H. X. Tang, M. L. Roukes, *Nat. Nanotechnol.* **2007**, *2*, 114.
- [24] E. Orhan, M. Yuksel, A. B. Ari, C. Yanik, U. Hatipoglu, A. M. Yağci, M. S. Hanay, *Front. Mech. Eng.* **2020**, *6*, 37.
- [25] R. T. Erdogan, M. Alkhaled, B. E. Kaynak, H. Alhmoud, H. S. Pisheh, M. Kelleci, I. Karakurt, C. Yanik, Z. B. Şen, B. Sari, A. M. Yagci, A. Özkul, M. S. Hanay, *ACS Nano* **2022**, *16*, 3821.
- [26] A. B. Ari, M. S. Hanay, M. R. Paul, K. L. Ekinci, *Nano Lett.* **2021**, *21*, 375.
- [27] C. Ti, A. B. Ari, M. Ç. Karakan, C. Yanik, I. I. Kaya, M. S. Hanay, O. Svitelskiy, M. González, H. Seren, K. L. Ekinci, *Nano Lett.* **2021**, *21*, 6533.
- [28] Y. Yamazaki, K. Kinoshita, *Adv. Sci.* **2024**, *11*, 2304804.
- [29] T. Zheng, W. Yang, J. Sun, X. Xiong, Z. Wang, Z. Li, X. Zou, *Sensors* **2021**, *21*, 2961.
- [30] M. P. Abrahams, J. Martinez, P. G. Steeneken, G. J. Verbiest, *Nano Lett.* **2024**, *24*, 14162.
- [31] D. Moreno-Garcia, X. Fan, A. D. Smith, M. C. Lemme, V. Messina, C. Martin-Olmos, F. Niklaus, L. G. Villanueva, *Small* **2022**, *18*, 2201816.
- [32] X. C. Zhang, E. B. Myers, J. E. Sader, M. L. Roukes, *Nano Lett.* **2013**, *13*, 1528.
- [33] R. G. West, K. Kanellopoulos, S. Schmid, *J. Phys. Chem. C* **2023**, *127*, 21915.
- [34] G. Dion, A. I.-E. Oudrhiri, B. Barazani, A. Tessier-Poirier, J. Sylvestre, in *Reservoir Computing: Theory, Physical Implementations, and Applications*, (Eds: K. Nakajima, I. Fischer), Springer Singapore, Singapore **2021**, ISBN: 9789811316876.
- [35] B. Barazani, G. Dion, J.-F. Morissette, L. J. Sylvestre, *J. Microelectromechanical Syst.* **2020**, *29*, 338.
- [36] Z. Zhang, X. Zhao, X. Zhang, X. Hou, X. Ma, S. Tang, Y. Zhang, G. Xu, Q. Liu, S. Long, *Nat. Comm.* **2022**, *13*, 6590.
- [37] A. H. Jaafar, L. Shao, P. Dai, T. Zhang, Y. Han, R. Beanland, N. T. Kemp, P. N. Bartlett, A. L. Hector, R. Huang, *Nanoscale* **2022**, *14*, 17170.
- [38] W. Sun, W. Zhang, J. Yu, et al., in *2022 IEEE Symposium on VLSI Technology and Circuits (VLSI Technology and Circuits)*, IEEE, Honolulu, HI **2022**, p. 222.
- [39] X. Zhu, Q. Wang, W. D. Lu, *Nat. Comm.* **2020**, *11*, 2439.
- [40] W. Jjiang, L. Chen, K. Zhou, L. Li, Q. Fu, Y. Du, R. Liu, *Appl. Phys. Lett.* **2019**, *115*, 192403.
- [41] K. Liu, T. Zhang, B. Dang, L. Bao, L. Xu, C. Cheng, Z. Yang, R. Huang, Y. Yang, *Nat. Electron.* **2022**, *5*, 761.
- [42] M. Cucchi, C. Gruener, L. Petrauskas, P. Steiner, H. Tseng, A. Fischer, B. Penkovsky, C. Matthus, P. Birkholz, H. Kleemann, K. Leo, *Sci. Adv.* **2021**, *7*, eabh0693.
- [43] Z. Chen, W. Li, Z. Fan, S. Dong, Y. Chen, M. Qin, M. Zeng, X. Lu, G. Zhou, X. Gao, J.-M. Liu, *Nat. Comm.* **2023**, *14*, 3585.
- [44] M. Tang, X. Zhan, S. Wu, M. Bai, Y. Feng, G. Zhao, J. Wu, J. Chai, H. Xu, X. Wang, J. Chen, *IEEE Electron Device Lett.* **2022**, *43*, 1555.
- [45] K. Kanno, A. Uchida, in *Reservoir Computing: Theory, Physical Implementations, and Applications* (Eds: K. Nakajima, I. Fischer), Springer Singapore, Singapore **2021**, ISBN: 9811316864.
- [46] M. Riou, J. Torrejon, F. Abreu Araujo, S. Tsunegi, G. Khalsa, D. Querlioz, P. Bortolotti, N. Leroux, D. Marković, V. Cross, K. Yakushiji, A. Fukushima, H. Kubota, S. Yuasa, M. Stiles, J. Grollier in *Reservoir Computing: Theory, Physical Implementations, And Applications*, (Eds: K. Nakajima, I. Fischer), Springer Singapore, Singapore **2021**, ISBN: 9811316864.
- [47] T. Taniguchi, S. Tsunegi, S. Miwa, K. Fujii, H. Kubota, K. Nakajima, in *Reservoir Computing: Theory, Physical Implementations, and Applications*, (Eds: K. Nakajima, I. Fischer), Springer Singapore, Singapore **2021**, ISBN: 9811316864.
- [48] N. Akashi, T. Yamaguchi, S. Tsunegi, T. Taniguchi, M. Nishida, R. Sakurai, Y. Wakao, K. Nakajima, *Phys. Rev. Res.* **2020**, *2*, 043303.
- [49] D. Marković, N. Leroux, M. Riou, F. Abreu Araujo, J. Torrejon, D. Querlioz, A. Fukushima, S. Yuasa, J. Trastoy, P. Bortolotti, J. Grollier, *Appl. Phys. Lett.* **2019**, *114*, 012409.
- [50] R. Nakane, A. Hirose, G. Tanaka, *Phys. Rev. Res.* **2021**, *3*, 033243.